

Automatic Segmentation of MR Images of the Developing Newborn Brain

Marcel Prastawa^{a,*} John H. Gilmore^b Weili Lin^c
Guido Gerig^{a,b}

^a*Department of Computer Science*

^b*Department of Psychiatry*

^c*Department of Radiology*

University of North Carolina, Chapel Hill, NC 27599, USA

Abstract

This paper describes an automatic tissue segmentation method for newborn brains from magnetic resonance images (MRI). The analysis and study of newborn brain MRI is of great interest due to its potential for studying early growth patterns and morphological changes in neurodevelopmental disorders. Automatic segmentation of newborn MRI is a challenging task mainly due to the low intensity contrast and the growth process of the white matter tissue. Newborn white matter tissue undergoes a rapid myelination process, where the nerves are covered in myelin sheathes. It is necessary to identify the white matter tissue as myelinated or non-myelinated regions. The degree of myelination is a fractional voxel property that represents regional changes of white matter as a function of age. Our method makes use of a registered probabilistic brain atlas. The method first uses robust graph clustering and parameter estimation to find the initial intensity distributions. The distribution estimates are then used together with the spatial priors to perform bias correction. Finally, the method refines the segmentation using training sample pruning and non-parametric kernel density estimation. Our results show that the method is able to segment the major brain structures, identifying myelinated and non-myelinated white matter regions.

Key words: Automatic brain MRI classification, Automatic brain MRI segmentation, Early Brain Development, Kernel density estimation, Neonatal MRI, Robust estimation

1 Introduction

The segmentation of newborn brain structures from magnetic resonance images (MRI) is crucial for the study of normal development and comparison to neurodevelopmental disorders at early stages. The development of new segmentation methods for this age group is driven by the increasing use of MRI to study newborns, for example our ongoing study of early brain development in normal and high risk children (Zhai et al., 2003; Gilmore et al., 2004) and the lack of appropriate segmentation methodology. Manual segmentation of newborn brains is tedious, time consuming, and lacks reproducibility. Therefore, it is necessary to use automatic segmentation methods for clinical studies with multiple subjects. This task is considerably more challenging compared to automatic segmentation of adult brain MRI due to the early development process; (Rutherford, 2002) provides an excellent description of newborn MRI and the dynamic changes seen over the early development period. In newborn infant brains, the white matter structure still undergoes myelination, where the fibers are being covered in myelin sheathes. Myelin is vital in the transmission of signals to different parts of the brain. The white matter structure at birth is generally not myelinated, except a few regions in the posterior limb of the internal capsule and parts of the brain stem. This is observable in the MR images, where the white matter appears with two different intensity characteristics (Figure 1). The non-myelinated white matter appears with inverse contrast compared to fully developed white matter. Over the first year, white matter becomes increasingly myelinated and shows significant changes of local contrast. The myelination process results in a reversal of white and gray matter contrast, which occurs at different times for different brain regions.

Several methods have been developed for automatically segmenting healthy adult brain MRI, mostly variations of multi-variate statistical classification techniques. Wells et al. (Wells et al., 1996) proposed an Expectation-Maximization scheme that interleaves segmentation and intensity bias correction. This method was extended by Van Leemput et al. (Van Leemput et al., 1999b) through the use of a probabilistic brain atlas. Warfield et al. (Warfield et al., 2000) described a k-nearest neighbor classification algorithm that is combined with template matching. Cocosco et al. (Cocosco et al., 2003) uses robust sample selection through minimum spanning trees for intensity-based classification. Automatic segmentation methods for healthy adult brain MRI typically fail in segmenting all the different structures apparent in newborn brain MRI,

* This research is supported by the the UNC Schizophrenia Research Center, an NIMH Conte Center MH064065 (PI J. A. Lieberman and J.H. Gilmore) and the UNC Neurodevelopmental Disorders Research Center HD 03110 (PI J. Piven). Marcel Prastawa is supported by R01 HL69808 NIH-NCI (PI E. Bullitt).

* Corresponding author. Address: CB #3175 Sitterson Hall, Chapel Hill, NC 27599
Email address: prastawa@cs.unc.edu (Marcel Prastawa).

particularly the myelinated white matter regions. A different class of segmentation techniques uses deformable templates that transfer the labeling of a template to each new subject. For example, the work by Collins et al. (Collins et al., 1999) which combines neural network classification with nonlinear image matching.

Previous work in segmentation of infant MRI was shown in (Matsuzawa et al., 2001), as part of a study of early brain development. Their method does not identify myelinated white matter and non-myelinated white matter separately. The results show that their method has difficulties dealing with tissue separation. Hüppi et al. (Hüppi et al., 1998) showed segmentation results of newborn infants, using the method of Warfield et al. (Warfield et al., 2000). Their subjects are mostly premature born infants with simpler cortical folding compared to normal newborns. The segmentation method identifies both non-myelinated and myelinated white matter.

Automatic segmentation of newborn brain MRI is significantly more challenging than the segmentation of adult brain MRI. This is mainly due to the biology and the rapid growth process. The specific challenges are:

- (1) The white matter and gray matter contrast to noise ratio (CNR) for newborn MRI can be as low as half of the one for adult brain MRI. A factor that reduces CNR is the small size of the infant brains. This requires them to be scanned at higher resolution, which leads to higher noise levels. The low CNR causes some difficulty in segmenting the partial volume regions.
- (2) Typically, newborn brain MRI exhibits some motion artifacts. The infants may not stay motionless during the scan period. This problem can be difficult to solve since the infants are not mentally aware, and healthy infants should not be sedated or restrained.
- (3) The process of myelination separates white matter tissue into two types. Myelination of white matter is a fractional property, where the dividing boundaries between regions that are fully myelinated and non-myelinated are ambiguous (Rutherford, 2002). The myelinated white matter regions are mostly distributed near the spine (central posterior) and parts of the internal capsule. We also observed the presence of myelinated white matter around the regions associated with the sensory and motor cortex.
- (4) Each tissue type in newborn brain MRI exhibits significant levels of intensity inhomogeneity and variability, which may be due to a combination of the RF inhomogeneity and biological properties of the developing tissue (Kandel et al., 2000).
- (5) The different tissues have large overlaps in their intensity characteristics, as shown in Figure 2. The decision boundaries for intensity-based classification are typically ambiguous and complex.

We developed an atlas based segmentation algorithm for newborn brain MRI that addresses the challenges listed above. The method uses the robust clustering method proposed by Cocosco et al. (Cocosco et al., 2003) and the robust parameter estimation method by Rousseeuw et al. (Rousseeuw and Van Driessen, 1999) to deal with noisy data. It uses the intensity inhomogeneity estimation scheme from spatial classification proposed by van Leemput et al. (Van Leemput et al., 1999a). The complex decision boundaries are modeled using non-parametric kernel density estimates, using the efficient method of Girolami et al. (Girolami and He, 2003). The probabilistic atlas is used as a spatial prior in the classification process as proposed by (Van Leemput et al., 1999a).

2 Method

Due to the large overlap in the tissue intensity distributions, we believe that it is necessary to use spatial priors in the segmentation. The spatial priors that we use is part of a probabilistic brain atlas of newborn MRI, shown in Figure 5. The atlas provides voxel prior probabilities for white matter, gray matter, and cerebrospinal fluid (csf). Myelinated white matter and non-myelinated white matter are combined as one white matter class in the atlas. This is necessary because it is difficult to model the different dynamic growth patterns across subjects with the significant changes during early brain development. With the combined white matter prior, the discrimination between the two different white matter classes is primarily driven by the image intensities. The atlas was created by averaging three co-registered semi-automatic segmentations. Each segmentation was done by a human rater that selects samples for each tissue types for k-nearest neighbor segmentation. The output of the k-nearest neighbor classification is then edited manually to remove possible errors. We use an additional blurring of the average segmentations to simulate a higher level of population variability.

Our segmentation framework is composed of three major steps, as shown in Figure 3. First, it obtains rough estimates of the class intensity clusters. It then iteratively performs inhomogeneity correction and parametric classification. Finally, it refines the segmentation using non-parametric kernel density estimates.

Before segmentation, we register the atlas to the subject using affine transformation and the mutual information image match metric (Maes et al., 1997). The registered images are filtered using anisotropic diffusion (Gerig et al., 1992).

2.1 Robust Intensity Distribution Estimation

The segmentation of newborn brain MRI involves classifying each voxel into different categories C , where C is commonly defined to be {myelinated white matter, non-myelinated white matter, gray matter, and cerebrospinal fluid}. The first step in the segmentation process is to determine the rough estimates of the class intensity distributions. We obtain samples for class C_i at location \vec{x} with high prior probability values, for example $Pr(C_i, \vec{x}) > 0.9$.

The white matter samples are constrained to have low image gradient magnitude values to avoid choosing samples near the transition regions between myelinated and non-myelinated white matter and at white/gray matter boundaries. The value we use for the gradient magnitude of our 3-D images is the 2-norm of the vector of individual gradient magnitudes, where

$$G(\vec{x}) = \sqrt{|\nabla I_1(\vec{x})|^2 + \dots + |\nabla I_n(\vec{x})|^2}$$

We only retain samples for the white matter class with $G(\vec{x})$ lower than the average of $G(\vec{x})$ over the white matter prior, $\gamma = \frac{\sum_{\vec{x}} Pr(\text{white matter}, \vec{x}) G(\vec{x})}{\sum_{\vec{x}} Pr(\text{white matter}, \vec{x})}$. The 2-norm gradient magnitude metric is more sensitive to noise compared to the vector field gradient magnitude metric described in (Lee and Cok, 1991). This is a desired property since we want to avoid sampling noisy regions.

We then process the obtained samples to remove outliers and false positives. We use the Minimum Covariance Determinant (MCD) estimator (Rousseeuw and Van Driessen, 1999) to generate the robust mean and covariance estimates of the unimodal distributions (gray matter and csf). The MCD estimator computes the robust mean and covariance that have the smallest determinant of covariance and covers at least half of the data. For the bi-modal white matter distribution, we use a robust graph based clustering method, similar to the one described in (Cocosco et al., 2003). The clustering method creates the Minimum Spanning Tree (MST) structure (Cormen et al., 2001) of the sample points and breaks the long edges to form the clusters (Duda et al., 2001). The removal of high gradient voxels helps in the clustering process, as shown in Figure 4.

The algorithm estimates the mean and covariance for myelinated white matter and non-myelinated white matter by iteratively breaking long edges of the MST. At each iteration, we break an undirected edge $e(v, w)$ that connects vertices v and w if it is longer than $A(v) \times T$ or $A(w) \times T$. $A(v)$ is the average length of edges incident on vertex v , $A(v) = \frac{1}{n_s} \sum_s |e(v, s)|$, while T is a distance multiplier. The iterative algorithm terminates when two clusters are found with intensity location estimates that are in the proper order. For example, the order of intensities for the classes in T2w from darkest to brightest

is myelinated white matter, gray matter, non-myelinated white matter, and csf.

The intensity location are estimated as the robust mean values computed with the MCD estimator. We use the robust MCD mean values, as opposed to the standard location estimates such as the mean or median, to make sure that we obtain reasonable sample clusters. The standard location estimates such as mean or median may not always be optimal for the noisy newborn MRI data. The mean value can be skewed by a single outlier sample, while the median value only uses one sample point and ignores contributions of other samples. The steps involved in the intensity distribution estimation are listed in Algorithm 1.

Algorithm 1. Initial intensity distribution estimation

- 1: Obtain samples by thresholding atlas prior probabilities
 - 2: Remove white matter samples with gradient magnitude higher than γ
 - 3: Compute robust mean intensity values for gray matter and csf (μ_{gm} and μ_{csf}) using the MCD estimator
 - 4: Construct Minimum Spanning Tree from white matter samples
 - 5: $T \leftarrow 2$
 - 6: **repeat**
 - 7: Break edges longer than $T \times A$, where A is the average length of connected neighbor edges
 - 8: Find largest myelinated white matter cluster, where $\mu_{myelinated} < \mu_{gm}$ in T2w
 - 9: Find largest non-myelinated white matter cluster, where $\mu_{gm} < \mu_{non-myelinated} < \mu_{csf}$ in T2w
 - 10: $T \leftarrow T - 0.01$
 - 11: **until** both white matter clusters are found or $T \leq 1$
 - 12: Compute white matter Gaussian distribution parameters from detected clusters
-

2.2 Inhomogeneity Correction

Newborn brain MRI exhibit higher intensity variability for each tissue and low intensity contrast compared to adult brain MRI. These two factors severely hamper the estimation of intensity inhomogeneity. Histogram based intensity inhomogeneity estimation methods, such as the ones proposed by Sled et al. (Sled et al., 1998) and Styner et al. (Styner et al., 2000), are likely to have difficulties in obtaining the optimal solution. The histogram of a newborn brain MR image is generally smooth with weak maximas.

In the case of inhomogeneity correction of newborn brain MRI, the spatial information is useful to deal with the low intensity contrast. We have chosen

to use the method developed by Van Leemput et al. (Van Leemput et al., 1999a). The scheme uses the spatial posterior probabilities to estimate the intensity inhomogeneity, which helps to overcome problems with low contrast and high variability. The inhomogeneity estimation method is an iterative generalized expectation maximization algorithm. It interleaves classification with inhomogeneity estimation at each iteration. The Gaussian distributions obtained from the previous segmentation step are used as initial parameters for the iterative inhomogeneity estimation algorithm.

The intensity likelihoods are modeled using parametric Gaussian functions, and the inhomogeneity is modeled using polynomials:

$$p(\vec{I}(\vec{x})|C_i) = \phi_{\Sigma_i}(\vec{I}(\vec{x}) - \mu_i - \sum_k \beta_k q_k(\vec{x}))$$

where ϕ is the Gaussian function, with mean μ_i and covariance Σ_i , the intensity inhomogeneity is the linear combination of the coefficients β_k and the basis polynomials q_k . The intensity inhomogeneity is estimated by least squares fitting of the polynomial coefficients to the log difference of the original image and the reconstructed image. The reconstructed image is the homogeneous image computed using the mean values μ_i and the posterior probabilities. The posterior probabilities are computed using the atlas prior probabilities:

$$p(C_i|\vec{I}(\vec{x})) = \frac{\sum_i p(\vec{I}(\vec{x})|C_i)Pr(C_i, \vec{x})}{\sum_i Pr(C_i, \vec{x})}$$

2.3 Segmentation Refinement Using Kernel Density Estimation

Modeling tissue intensity distributions as Gaussian probability density functions for the segmentation and inhomogeneity correction are often a first choice but not always optimal. In the presence of complex classification decision boundaries, Gaussian distribution functions show significant overlap and are not properly modeling cluster shapes. In order to refine the classification, we sample the inhomogeneity corrected images, prune the outliers and false positives from the samples, and then estimate the intensity distribution using kernel density functions (Duda et al., 2001; Hastie et al., 2001).

The intensity probability density function for each class is estimated as follows:

$$\hat{p}(\vec{I}(\vec{x})|C_i) = \sum_{j=1}^{N_i} w_{ij} K_h(\vec{I}(\vec{x}) - T_{ij})$$

where K_h is the Gaussian kernel with standard deviation h , N_i is the number of training samples for class C_i , and T_{ij} is the j^{th} training sample for the i^{th} class. Each training sample has an associated weight w_{ij} , where for each class

C_i , $\sum_{j=1}^{N_i} w_{ij} = 1$. The kernel density estimates are used to produce the final classification result, the class posterior probabilities:

$$\hat{p}(C_i|\vec{I}(\vec{x})) = \frac{\sum_i \hat{p}(\vec{I}(\vec{x})|C_i)Pr(C_i, \vec{x})}{\sum_i Pr(C_i, \vec{x})}$$

The atlas prior probabilities are also used at this stage, to overcome some of the ambiguities in the decision boundaries for image intensities by using spatial information.

The set of training samples T for the kernel density estimates are obtained by sampling the MR images using the previously obtained posterior probabilities. Each sample T_{ij} is obtained by selecting features at location \vec{x} where

$$\arg \max_{C_k} p(C_k|\vec{I}(\vec{x})) = C_i$$

The samples are pruned using the robust MST pruning strategy proposed by Cocosco et al. (Cocosco et al., 2003). This is done to remove the false positives and outliers that we may obtain by using Gaussian distribution estimates in the previous step.

The method proposed by Girolami et al. (Girolami and He, 2003) is used to efficiently estimate the kernel density function. This method speeds up the density estimation process by reducing the size of the training set. The weights $w_{i,j}$ are chosen to minimize the integrated squared error between the true density function and the estimated kernel density function. Redundant training features are assigned lower weight values compared to characteristic training features. This minimization process for the sample weight assignment is similar to the quadratic optimization process for Support Vector Machines, for which an efficient solution exists (Schölkopf et al., 2001). The samples with zero weights are removed from the training set, which effectively removes the redundant features in the training set. Compared to other fast density estimation techniques such as pre-binning (Scott and Sheather, 1985) and multi-scale selection using hyperdiscs (Mitra et al., 2002), this method has the advantage of having only one user specified parameter: the kernel width or the standard deviation of the Gaussian kernels.

3 Results

We have applied our segmentation method to four different subjects (Figure 6) , with the results shown in Figures 7, 8, 9, and 10. The volumes for each segmented structures are listed in Figure 11. These four cases are samples from a large neonatal study at UNC Chapel Hill to assess early brain development

in normal and high risk children (Zhai et al., 2003; Gilmore et al., 2004). We currently have over 50 datasets of neonatal MRI and will collect a total of 125, with some of them followed-up at the age of one year. As part of the study, we plan to measure the cortical folding and the cortical thickness of the newborn brains. Figure 12 shows the 3D view of the relevant structures for one of the subjects.

Images were acquired on a Siemens head-only 3T scanner (Allegra, Siemens Medical System, Erlangen, Germany). Two structural imaging sequences were used: a magnetization prepared rapid gradient echo (MPRAGE) T1-weighted and a turbo spin echo (TSE), dual-echo (proton density and T2 weighted). Total scan time for structural scans was approximately 10 minutes. The imaging parameters for the MP-RAGE sequence were: repeat time TR = 11.1 ms, echo time TE = 4.3 ms, inversion time TI = 400 ms, slice thickness TH = 1 mm, in-plane resolution = $0.898 \times 0.898 \text{ mm}^2$. A total of 128 sagittal images were acquired to cover the entire brain. The imaging parameters for the TSE sequence were: TR = 7 s, TE = 15 and 90 ms, TH = 1.95 mm, in-plane resolution $1.25 \times 1.25 \text{ mm}^2$, and 56 slices.

Visual inspection shows that the majority of the brain regions are properly classified, although the distinction between myelinated white matter and non-myelinated white matter could need improvement in some regions. The myelinated white matter regions are mostly distributed near the spine (central posterior) and internal capsule. We also observed the presence of small regions of myelinated white matter around the regions associated with the sensory and motor cortex.

At this point, we are unable to provide quantitative validation of the segmentation results due to the lack of a gold standard. The common standard, manual segmentations, would be difficult to obtain since highly convoluted structures in low-contrast, noisy data are very hard to trace. In addition to that, the myelinated white matter and the non-myelinated white matter have ambiguous boundaries, which would make manual segmentation results highly variable and difficult to reproduce. This problem is solved for adult brain MRI by using web-based archives with simulated datasets (Cocosco et al., 1997; Collins et al., 1998) and manually segmented real datasets (MGH, 2004). Both types of validation test data are currently not available for newborn brain MRI data. Reproducibility is optimal since the method is fully automatic.

4 Discussion

We have presented an atlas-based automatic segmentation method for multi-channel newborn brain MRI. The method uses graph clustering and robust

estimation to obtain initial distribution estimates from the noisy data. These estimates are then used to generate spatial posterior probabilities for correcting the intensity inhomogeneity inherent in the image. The segmentation is then refined through the use of non-parametric kernel density estimates.

The use of a probabilistic atlas or a template such as the one used in (Warfield et al., 2000) is essential to overcome the intensity contrast limitations. A probabilistic brain atlas that captures the variability of the large population is essential for the proposed method, such as the one described in (Evans et al., 1993) for adult brain MRI. The creation of a true newborn brain atlas requires the segmentations of a large set of representative data. Also, with the high level of brain shape variability in infants, it is likely that a non-linear registration will be required for a reliable atlas formation. These factors make the creation of a newborn brain atlas highly challenging. The current atlas that is created from a small set of data seems sufficient for our data. However, we are working on an improved atlas that shows better population variability.

The results shows that the major structures are properly segmented, while the separation of myelinated and non-myelinated white matter still lacks spatial coherence in some regions. The segmentations of regions largely affected by partial voluming is still insufficient and an inherent problem with voxel-based classification. Problems mostly occur in thin gray-csf cortical boundaries falsely classified as white matter. Due to the nature of the data, the tissue properties are difficult to discriminate and this exacerbates the problem. Illustrations of segmentations of the four cases demonstrate that the new method can cope with variable brain shapes. Also, location and shape of the early myelination structures across the subjects seem quite similar. The new segmentation technique is currently applied to the whole database of over 50 neonates (age range is 42.7 ± 1.8 weeks of gestational age) to study volume and structure of brain tissue at this early age.

Another significant challenge in newborn brain MRI segmentation is the creation of a standard for validation. To our knowledge, there is no standard dataset available to the community to measure and compare the performance of segmentation methods. We are currently working on contour-based segmentation with subsequent manual interaction to provide standardized test data for segmentation validation.

Acknowledgments

We acknowledge Koen van Leemput for providing the MATLAB code that aids the development of the bias correction software and the Insight Toolkit community (Insight Consortium, 2004) for providing the software framework

for the segmentation algorithm.

References

- Cocosco, C. A., Kollokian, V., Kwan, R. K.-S., Evans, A. C., 1997. BrainWeb: Online interface to a 3D MRI simulated brain database. *NeuroImage* 5 (4).
- Cocosco, C. A., Zijdenbos, A. P., Evans, A. C., December 2003. A fully automatic and robust brain MRI tissue classification method. *Medical Image Analysis* 7, 513–527.
- Collins, D. L., Zijdenbos, A. P., Baaré, W. F. C., Evans, A. C., 1999. ANIMAL+INSECT: Improved cortical structure segmentation. In: Kuba, A., Sámal, M., Todd-Pokropek, A. (Eds.), *Information Processing in Medical Imaging*. Vol. 1613 of *Lecture Notes in Computer Science*. Springer, Heidelberg, Germany, pp. 210–223.
- Collins, D. L., Zijdenbos, A. P., Kollokian, V., Sled, J. G., Kabani, N. J., Holmes, C. J., Evans, A. C., June 1998. Design and construction of a realistic digital brain phantom. *IEEE TMI* 17 (3), 463–468.
- Cormen, T. H., Leiserson, C. E., Rivest, R. L., Stein, C., 2001. *Introduction to Algorithms*, 2nd Edition. MIT Press, Cambridge, MA.
- Duda, R. O., Hart, P. E., Stork, D., 2001. *Pattern Classification*, 2nd Edition. Wiley.
- Evans, A. C., Collins, D. L., Mills, S. R., Brown, E. D., Kelly, R. L., Peters, T. M., 1993. 3D statistical neuroanatomical models from 305 MRI volumes. In: *Proc. IEEE Nuclear Science Symposium and Medical Imaging Conference*. pp. 1813–1817.
- Gerig, G., Kübler, O., Kikinis, R., Jolesz, F., June 1992. Nonlinear anisotropic filtering of MRI data. *IEEE TMI* 11, 221–232.
- Gilmore, J., Zhai, G., Wilber, K., Smith, J., Lin, W., Gerig, G., 2004. 3T magnetic resonance imaging of the brain in newborns. *Psychiatry Research Neuroimaging* 132, 81–85.
- Girolami, M., He, C., October 2003. Probability density estimation from optimally condensed data samples. *IEEE Trans. Pattern Analysis and Machine Intelligence* 25 (10), 1253–1264.
- Hastie, T., Tibshirani, R., Friedman, J. H., 2001. *The Elements of Statistical Learning*. Springer-Verlag.
- Hüppi, P., Warfield, S., Kikinis, R., Barnes, P., Zientara, G., Jolesz, F., Tsuji, M., Volpe, J., 1998. Quantitative magnetic resonance imaging of brain development in premature and normal newborns. *Ann Neurol* 43, 224–235.
- Insight Consortium, 2004. *Insight Toolkit*.
URL <http://www.itk.org>
- Kandel, E. R., Schwartz, J. H., Jessel, T. M., 2000. *Principles of Neural Science*, 4th Edition. McGraw Hill.
- Lee, H. C., Cok, D. R., 1991. Detecting boundaries in a vector field. *IEEE*

- Trans. Signal Processing 39 (5), 1181–1194.
- Maes, F., Collignon, A., Vandermeulen, D., Marchal, G., Suetens, P., April 1997. Multimodality image registration by maximization of mutual information. *IEEE TMI* 16 (2), 187–198.
- Matsuzawa, J., Matsui, M., Konishi, T., Noguchi, K., Gur, R., Bilder, W., Miyawaki, T., April 2001. Age-related volumetric changes of brain gray and white matter in healthy infants and children. *Cerebral Cortex* 11 (4), 335–342.
- MGH, 2004. Internet Brain Segmentation Repository.
URL <http://www.cma.mgh.harvard.edu/ibsr>
- Mitra, P., Murthy, C. A., Pal, S. K., 2002. Density based multiscale data condensation. *IEEE Trans. Pattern Analysis and Machine Intelligence* 24 (6).
- Rousseeuw, P. J., Van Driessen, K., 1999. A fast algorithm for the minimum covariance determinant estimator. *Technometrics* 41 (3), 212–223.
- Rutherford, M. (Ed.), 2002. *MRI of the Neonatal Brain*. W.B. Saunders.
- Schölkopf, B., Platt, J., Shawe-Taylor, J., Smola, A., Williamson, R., 2001. Estimating the support of a high-dimensional distribution. *Neural Computation* 13, 1443–1471.
- Scott, D. W., Sheather, S. J., 1985. Kernel density estimation with binned data. *Comm Statistics- Theory and Methods* 14, 1353–1359.
- Sled, J. G., Zijdenbos, A. P., Evans, A. C., 1998. A nonparametric method for automatic correction of tissue nonuniformity in MRI data. *IEEE Trans. Medical Imaging* 17 (1), 87–97.
- Styner, M., Brechbuhler, C., Szekely, G., Gerig, G., 2000. Parametric estimate of intensity inhomogeneities applied to MRI. *IEEE TMI* 19 (3), 153–165.
- Van Leemput, K., Maes, F., Vandermeulen, D., Suetens, P., October 1999a. Automated model-based bias field correction of MR images of the brain. *IEEE Trans. Medical Imaging* 18, 885–896.
- Van Leemput, K., Maes, F., Vandermeulen, D., Suetens, P., October 1999b. Automated model-based tissue classification of MR images of the brain. *IEEE Trans. Medical Imaging* 18, 897–908.
- Warfield, S. K., Kaus, M., Jolesz, F. A., Kikinis, R., Mar 2000. Adaptive, template moderated, spatially varying statistical classification. *Medical Image Analysis* 4 (1), 43–55.
- Wells, W. M., Kikinis, R., Grimson, W. E. L., Jolesz, F., August 1996. Adaptive segmentation of MRI data. *IEEE Trans. Medical Imaging* 15, 429–442.
- Zhai, G., Lin, W., Wilber, K., Gerig, G., Gilmore, J. H., DEC 2003. Comparison of regional white matter diffusion in healthy neonates and adults using a 3T head-only MR scanner. *Radiology* 229, 673–681.

Figures

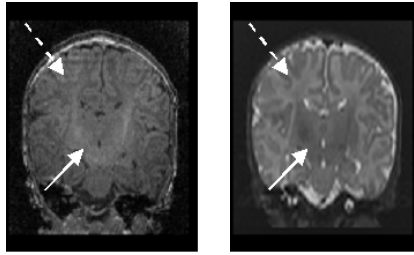


Fig. 1. MR images of a newborn brain (subject 0096, coronal view). Left: T1w image, right: T2w image. The arrows show the white matter structure. The arrow with the solid line indicates myelinated white matter, the arrow with the dashed line indicates non-myelinated white matter. Early myelination in white matter is shown as bright regions in the T1w image and dark regions in the T2w image.

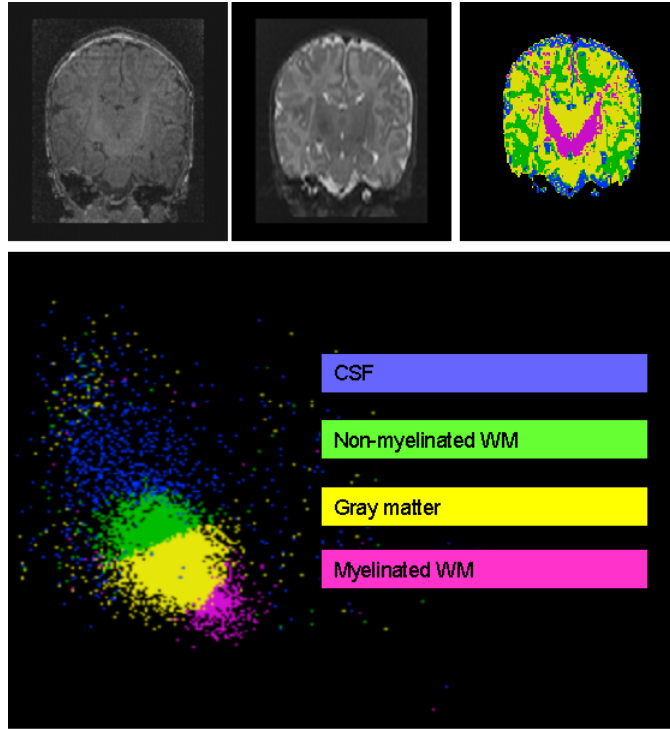


Fig. 2. MR intensity characteristics of a newborn brain (subject 0096, coronal view). Top, from left to right: T1w image, T2w image, and segmentation labels. Purple is myelinated white matter, yellow is gray matter, green is non-myelinated white matter, and blue is cerebrospinal fluid. Bottom: the scatterplot of the tissue intensities, the horizontal axis represents T1w intensities and the vertical axis represents T2w intensities. There is significant overlap between the intensities of different tissues, and there are ambiguities in the decision boundaries.

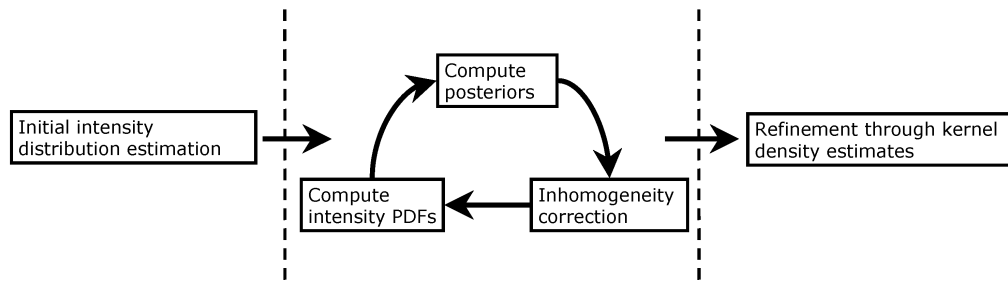


Fig. 3. The segmentation framework.

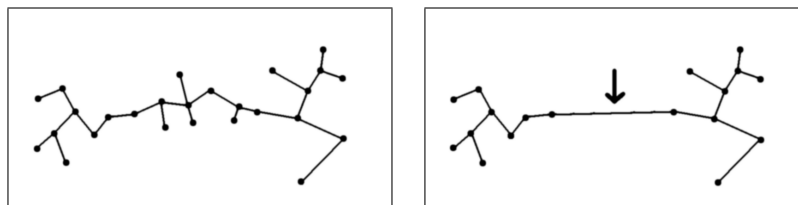


Fig. 4. Illustrations of the Minimum Spanning Trees for white matter obtained using different sampling strategies. Left: Samples with high probability values. Right: Samples with high probability values and low gradient magnitude. Choosing only samples with low gradient magnitude helps to remove samples from the transition regions between myelinated white matter and non-myelinated white matter and gray/white boundary voxels. This is crucial for clustering based on edge breaking. As seen on the right picture, breaking the longest edge marked by the arrow would give two well separated clusters.

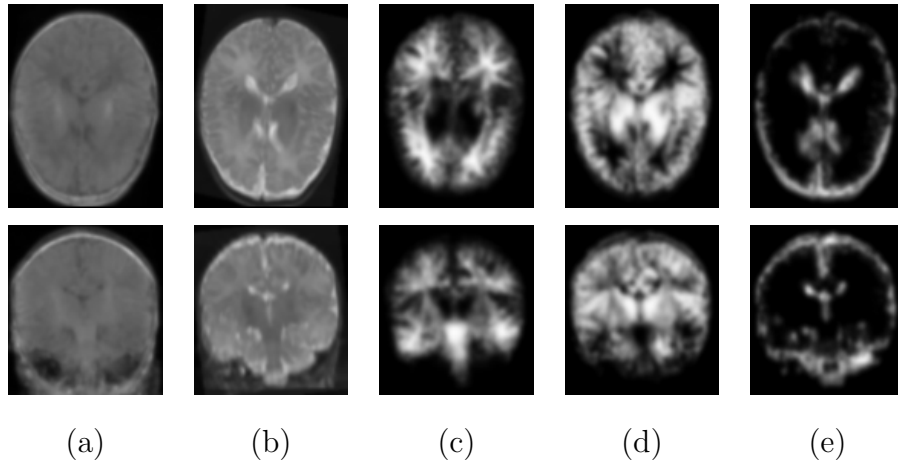


Fig. 5. The probabilistic brain atlas of a newborn brain. From left to right: (a) the T1w average image, (b) T2w average image, and prior probability values for (c) white matter (either myelinated or non-myelinated), (d) gray matter, and (e) csf. Top: axial view. Bottom: coronal view.

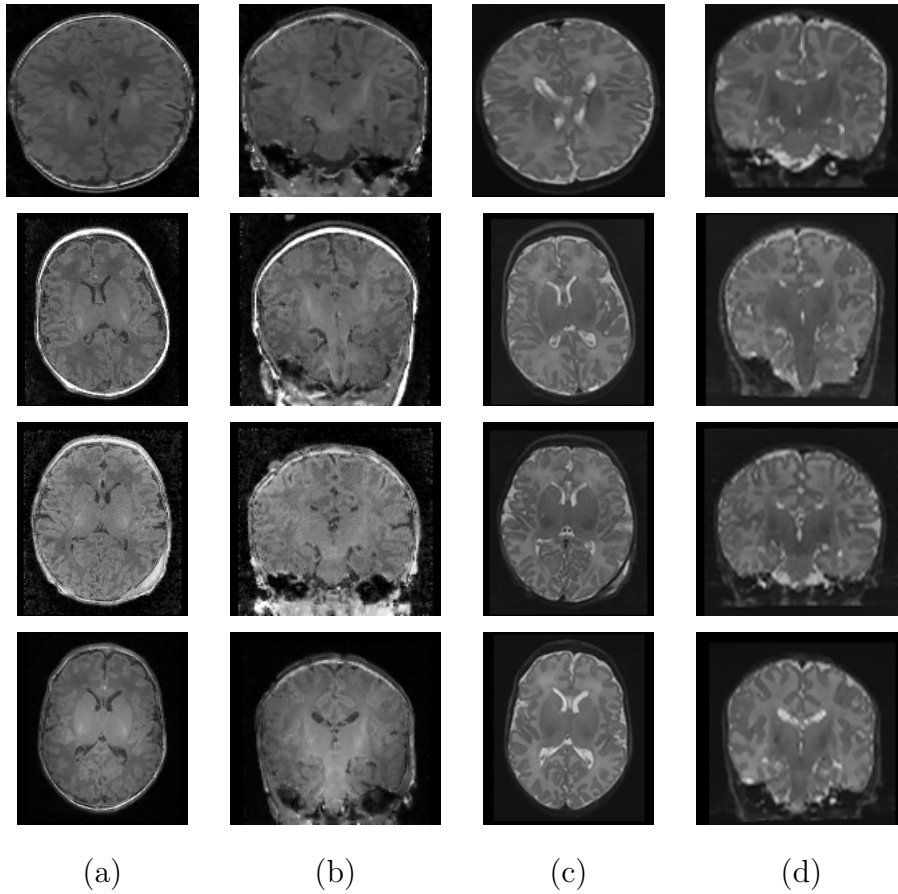


Fig. 6. MR images of the four different subjects. From left to right: (a) axial view of the T1w images, (b) coronal view of the T1w images, (c) axial view of the T2w images, and (d) coronal view of the T2w images. From top to bottom: subject 0096, 0117, 0118, and 0123.

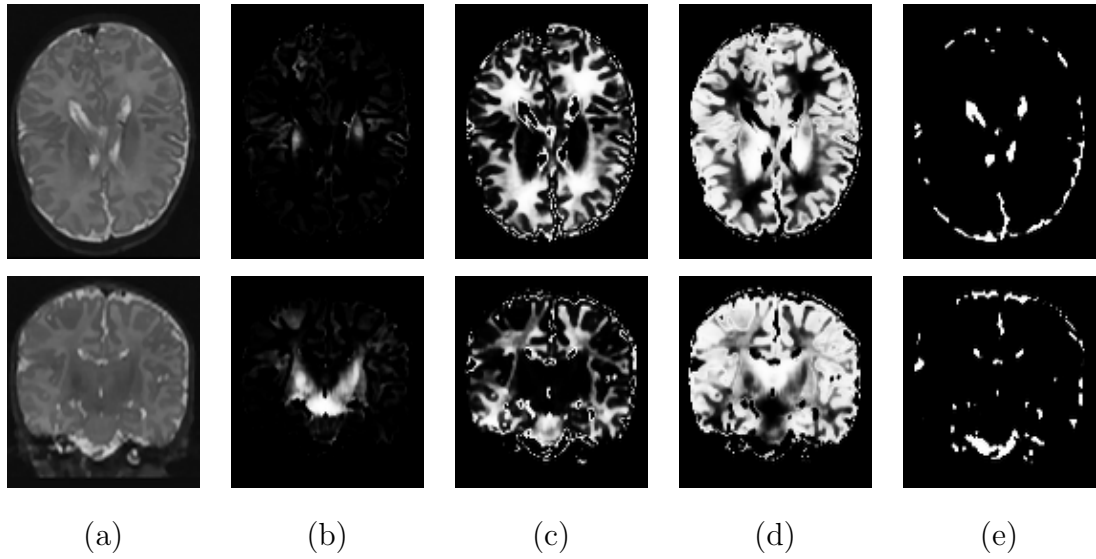


Fig. 7. The segmentation results for subject 0096. From left to right: (a) T2w image and the class posterior probabilities for (b) myelinated white matter, (c) non-myelinated white matter, (d) gray matter, and (e) cerebrospinal fluid. Top: axial view. Bottom: coronal view.

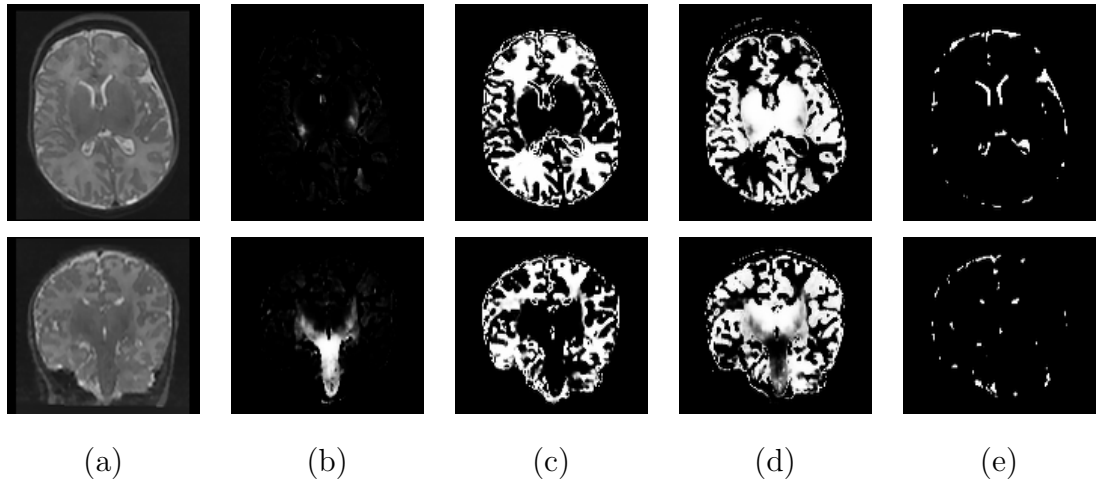


Fig. 8. The segmentation results for subject 0117. From left to right: (a) T2w image and the class posterior probabilities for (b) myelinated white matter, (c) non-myelinated white matter, (d) gray matter, and (e) cerebrospinal fluid. Top: axial view. Bottom: coronal view.

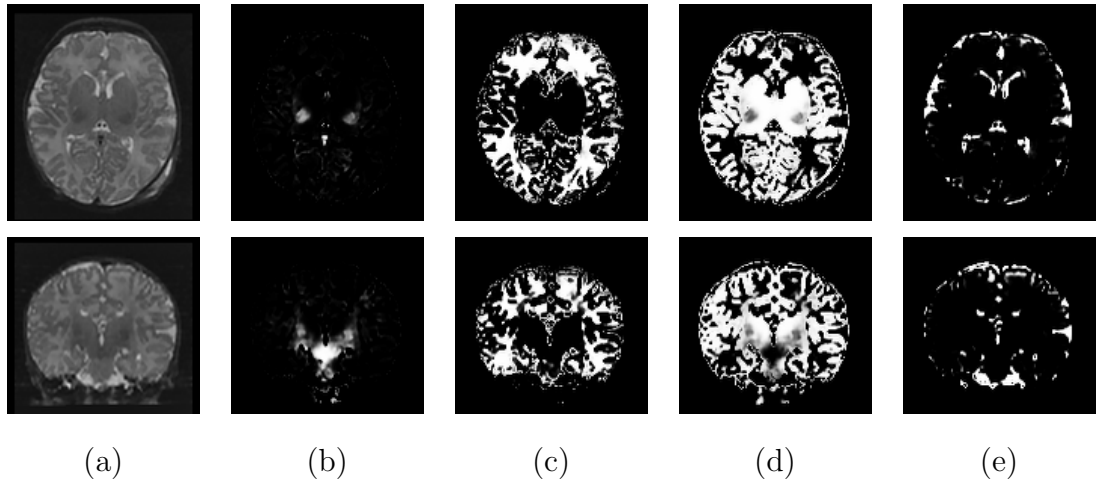


Fig. 9. The segmentation results for subject 0118. From left to right: (a) T2w image and the class posterior probabilities for (b) myelinated white matter, (c) non-myelinated white matter, (d) gray matter, and (e) cerebrospinal fluid. Top: axial view. Bottom: coronal view.

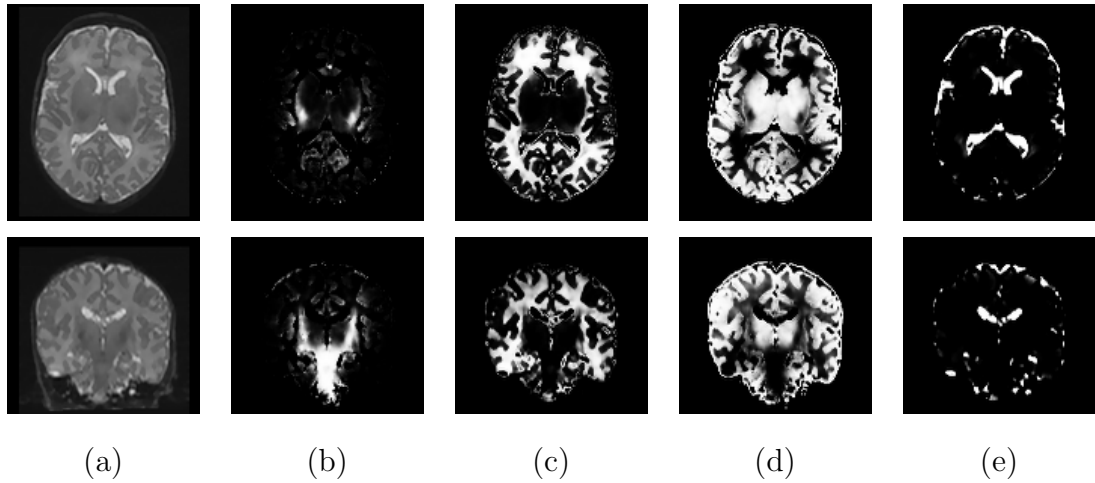


Fig. 10. The segmentation results for subject 0123. From left to right: (a) T2w image and the class posterior probabilities for (b) myelinated white matter, (c) non-myelinated white matter, (d) gray matter, and (e) cerebrospinal fluid. Top: axial view. Bottom: coronal view.

Subject	ICV	Myelinated WM	Non-myelinated WM	Gray Matter	CSF
0096	504724	15353	157160	289133	43078
0117	527885	12678	234706	250161	30340
0118	514760	11480	193307	255849	54124
0123	499775	28487	170227	252056	49005

Fig. 11. The volumes of the segmented structures for the four subjects. These include the intra cranial volume (ICV) and the volumes of the individual structures (myelinated white matter, non-myelinated white matter, gray matter, and cerebrospinal fluid). All volumes are measured in cubic millimeters.

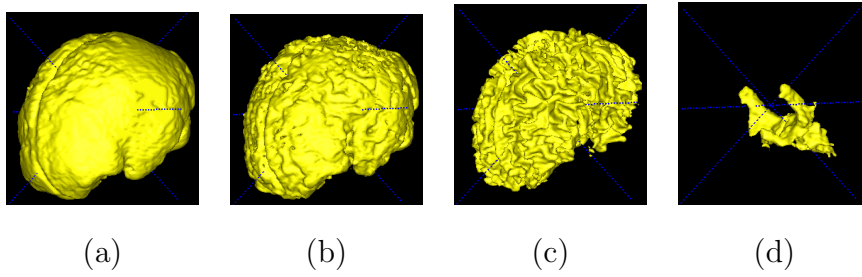


Fig. 12. Surface renderings of the segmented structures of subject 0096. From left to right: (a) intra cranial volume, (b) gray matter, (c) non-myelinated white matter, and (d) myelinated white matter.